FAST WIRE-MESH SENSORS FOR GAS-LIQUID FLOWS AND DECOMPOSITION OF GAS FRACTION PROFILES ACCORDING TO BUBBLE SIZE CLASSES

H.-M. Prasser, E. Krepper, D. Lucas, J. Zschau[1)], D. Peters, G. Pietzsch, W. Taubert, M. Trepte[2)]

[1)] Forschungszentrum Rossendorf e.V., P.O.Box 510119, D-01314 Dresden, Germany
e-mail: prasser@fz-rossendorf.de

[2)] Teletronic Ingenieurbüro GmbH, Bautzner Landstraße 45, D-01454 Großerkmannsdorf
e-mail: ttronic@teletronic.tz-rotech.de

1 Introduction

The described electrode-mesh sensor is based on a measurement of the local instantaneous conductivity of the two-phase mixture. Wire-mesh sensors were introduced by Johnson [1], who used them to measure the integral gas fraction in the cross section. Reinecke et al. [2] presented a device visualising sequences of gas fraction distributions with a rate of about 100 frames per second for the first time. It consists of three layers of electrode grids. Three independent projections of the gas fraction distribution in the sensor cross section are obtained by measuring the impedance between two adjacent parallel wires. The imaging is carried out applying tomographic reconstruction algorithms. Our own development was aimed at a direct conductivity measurement between pairs of crossing wires to avoid tomographic reconstruction algorithms [3] and to increase time resolution. The first generation of signal acquisition units worked at a framing rate of 1200 Hz. Recently, the second generation has achieved a time resolution of 10 000 frames per second [4].

Both types were used to study a vertical upwards air-water flow in a pipe of 51.2 mm diameter. The high resolution allows to derive bubble size distributions and gas fraction profiles decomposed according to bubble size classes. The processes of lateral movement of the bubbles due to the non-drag forces, the bubble coalescence and fragmentation were investigated by studying the evolution of these partial profiles along the pipe. The effect of lift force inverse at some critical diameter of the bubbles, predicted by [5], was clearly detected in a realistic, polydisperse two-phase flow. Especially with the second generation device, the structure of the two-phase flow in case of air and water velocities in the range of 10 m/s was visualised in detail for the first time.

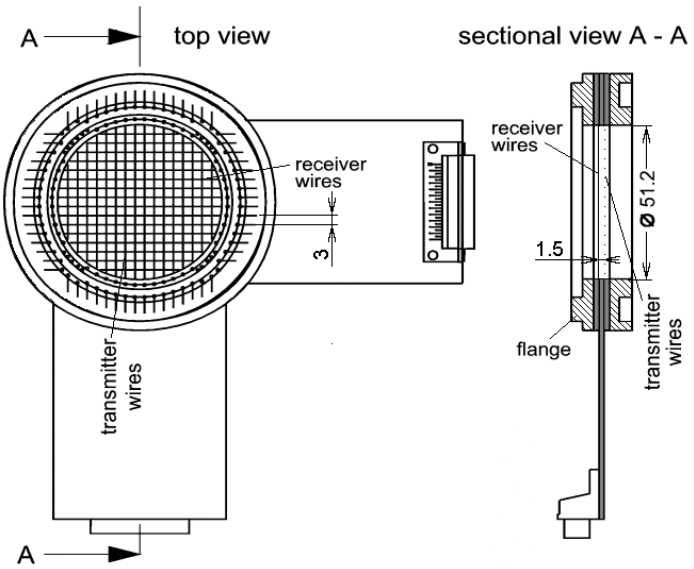

Fig. 1: Wire-mesh sensor with 2 x 16 electrodes

2 Function of the wire-mesh sensor

Our wire-mesh sensor consists of two electrode grids with 16 electrode wires (diameter 120 µm) each, placed at an axial distance of 1.5 mm behind each other (Fig. 1). The electrode pitch is 3 mm, which is determining the spatial resolution.

In order to explain the function, a simplified scheme of the sensor together with its electronic circuitry is shown in Fig. 2. Here, for simplicity, the number of electrodes is reduced to four in each plane. During the signal acquisition, one plane of electrode wires is used as transmitter, the other as receiver plane. The transmitter electrodes are activated by supplying them with voltage pulses in a successive order. This is done by closing one of the semiconductor switches S1 - S4 for the duration of the excitation pulse.

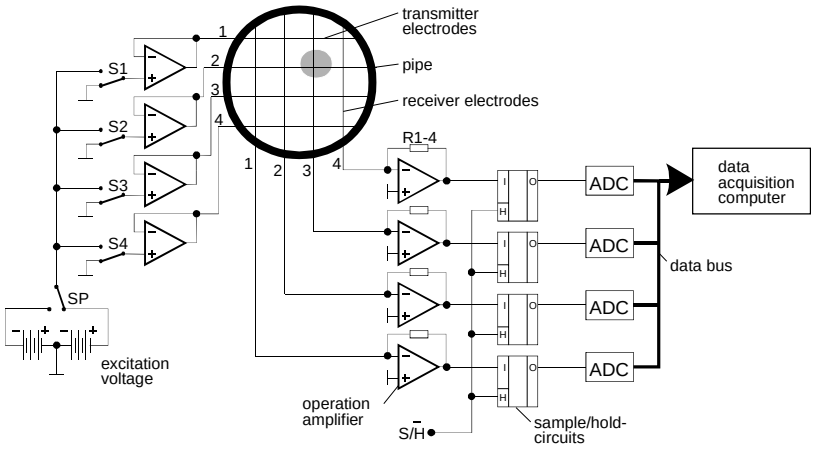

Fig. 2 Simplified scheme of wire-mesh sensor and signal acquisition electronics

To suppress electrode polarisation and electrolysis at the electrode, the excitation is carried out by putting a DC free symmetrical bipolar square-wave pulse on the transmitter electrode to be activated (signal U_{T2} in Fig. 3). For this purpose, the polarity is altered by changing switch SP after the first half period of the excitation pulse. The corresponding binary signals to control the switches are shown in Fig. 3.

Due to the imaginary component of the impedance of the ion layer at the electrodes, the sensor and the cable, the resulting currents arriving at the receiver wires show a transient behaviour (see signal I_{R2} in Fig. 3). These signals are pre-amplified and sampled by activating sample & hold circuits (S/H) at the end of the first half-period of the excitation pulse (signal S/H in Fig. 3). At this moment, the transient has settled and the output voltage of the S/H circuits is proportional to the real component of the received current. This

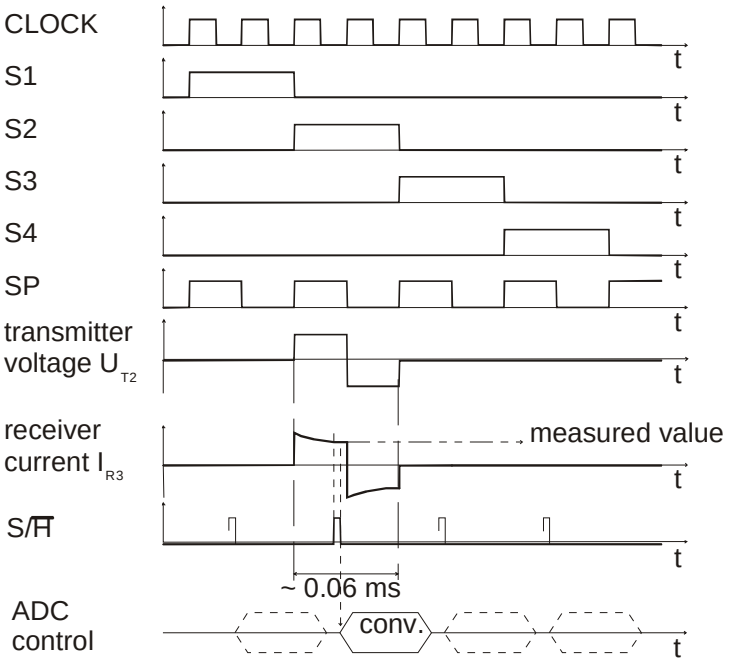

Fig. 3 Pulse diagram of the most important control signals of the signal acquisition electronics

has several advantages compared to a traditional AC excitation with a sinusoidal voltage, requiring a demodulation of the received alternating currents with a subsequent low-passing to remove the carrier frequency. The low-passing makes it necessary to apply a carrier frequency that is higher than the measuring rate by an order of magnitude, while in case of the square-wave excitation the excitation frequency and measuring rate can be equal. This helps to increase the measuring frequency to achieve high framing rates.

After the pre-amplification, the analogue signals are captured by the S/H circuits, digitalised by analogue/digital converters and stored in a data acquisition computer. This procedure is repeated for all transmitter electrodes. After activating the last transmitter wire, a complete matrix of measured values is stored in the computer (4 x 4 =16 values in case of the simplified sensor in Fig. 2, 16 x 16 = 256 values in case of 2 x 16 electrode wires), which represents the complete two-dimensional conductivity distribution in the sensor cross section. The local instantaneous conductivity is measured at each crossing point of a transmitter and a receiver wire independently. In case of the sensor shown in Fig. 1 there are 242 useful crossing points within the cross section of the sensor, the rest is located outside the circular measuring area.

The time sequence control of the measurement is carried out a device-specific FPGA (Freely Programmable Gate Array). For the data communication a parallel interface to the ISA bus of the PC with a bus width of 16 bit is used. A special interface card was developed, which has to be placed into the PC. The time sequence of the successive activation of the transmitter wires and the data transfer is controlled from the side of the PC. The interface card is linked with the signal acquisition unit of the wire-mesh sensor over an approximately 3 m long cable. The time sequence of the successive activation of the transmitter wires is controlled from the side of the PC. Before the measurement is started, a set of control words is transferred to the signal acquisition unit and stored in the FPGA. In these control words, the amplifying stages of the pre- and post-amplifier cascades are set, the number of electrodes in the wire mesh sensor and the excitation pulse width must be specified.

The length of the excitation pulse is programmable in the range from 3 to 19 µs. When a period of less than 0.06 ms is set, the total measuring cycle in case of 16 transmitter electrodes takes less than 1 ms. In the result, the time resolution achieved by the signal processing unit of the first generation is 1200 frames per second. This limit is also given by the capacity of the parallel interface used to transfer the data to the data acquisition PC.

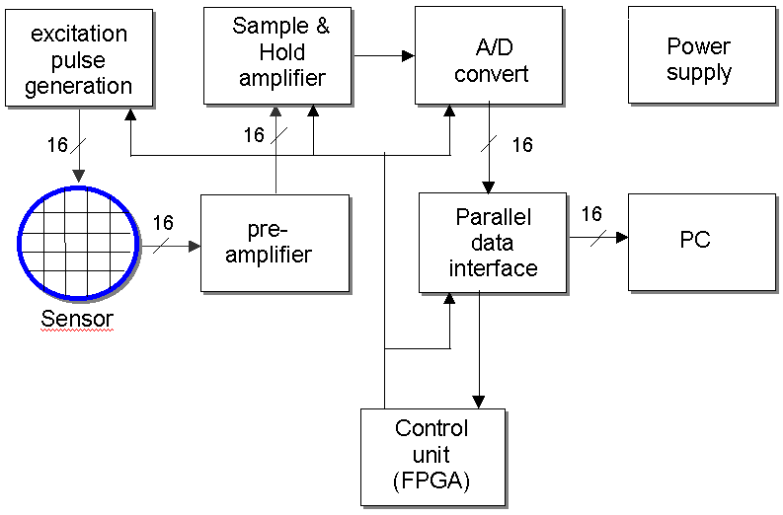

Fig. 4 Structural scheme of the signal acquisition unit for 1200 frames per second

An important feature is the suppression of cross-talk. A large part of the excitation current is flowing from the activated transmitter wire to the adjacent parallel non-activated transmitter wires. Cross talk may happen, if the potential of the non-activated electrodes departs from zero due to these parasitic currents, because the appearing potential difference causes currents from the non-activated transmitter electrodes to the receiver wires. This results in a loss of resolution (blurring) in the direction perpendicular to the transmitter wires. The similar may happen, if the currents arriving at the receiver wires are able to create a non-zero potential on the receivers. In this case, parasitic currents between adjacent parallel receiver wires occur and the image loses sharpness in the direction perpendicular to the receiver wires.

The cross-talk is sufficiently suppressed by applying driver circuits and pre-amplifiers with low output respectively input impedance to generate the excitation pulses and to measure the currents. In order to drive the transmission electrodes with an impedance as low as possible, an individual operational amplifier is foreseen for each electrode. The current entries at the receiver electrodes are converted in a voltage signal by operation amplifier (OPV) with small input bias current, switched as impedance converters. By the help of the low-impedance the potential of all transmitter and receiver wires except the currently activated one is kept on zero potential, so that parasitic currents cannot occur.

For a sufficient cross-talk suppression the impedance of the input and output cascades must be significantly less than the impedance of the sensor immersed into the measuring fluid. This leads to limitations concerning the maximum conductivity of the liquid phase. Without additional measures, the device can work at liquid conductivities up to approximately 1000 µS/cm (tap water quality), the lower limit is given by the sensitivity of the input cascades (0.1 µS/cm, distilled water). Only due to the cross-talk suppression it is possible to obtain instantaneous gas fraction distributions with a spatial resolution equal to the electrode pitch.

3 Second generation signal acquisition unit with 10 000 frames per second

For an increase of the measuring rate from 1200 frames/s to the desired 10 kHz it was necessary to decrease the build-up time of the preamplifiers and to speed-up the data transfer from the signal acquisition unit to the data acquisition PC. It turned out, that the high quantity of data produced at the 10 000 frames per second cannot be transferred on-line. In the consequence, the data acquisition module was equipped with an own memory unit. Furthermore, it was decided to modify the signal sampling by using both half-periods of the bipolar excitation pulse. For this purpose, the Sample & Hold circuits are activated at the end of both the positive and the negative half-periods. The results of both samplings are subtracted digitally after the A/D conversion. This technique allows to suppress low-frequency noise, such as 50 Hz mains disturbances.

These specifications led to a completely new conception with the following modifications in relation to the first device version. Main difference is the introduction of a DSP (digital signal processor) for the control of the measurement. The new structure is shown in the block diagram (Fig. 5). The new features are:

1. The entire signal acquisition procedure is operated autonomously, controlled by a DSP.

2. The measured data (up to 170.000 frames) are stored in a buffer memory controlled by the DSP.

3. The data transfer is between signal acquisition unit and data acquisition PC is carried out via an Ethernet interface.

4. The sixteen output cascades driving the transmitter electrodes and the current-to-voltage converter cascades of the preamplifiers were put into separate functional units, which are directly plugged to the connectors of the sensor. The cables carry pre-amplified signals, which helps to reduce noise.

5. The receiver signals are sampled during the positive and the negative half-period (see explanation above).

6. The signal processing after the A/D conversion, including the subtraction of the half-periods, is fully digital, it is carried out by a programmable FPGA.

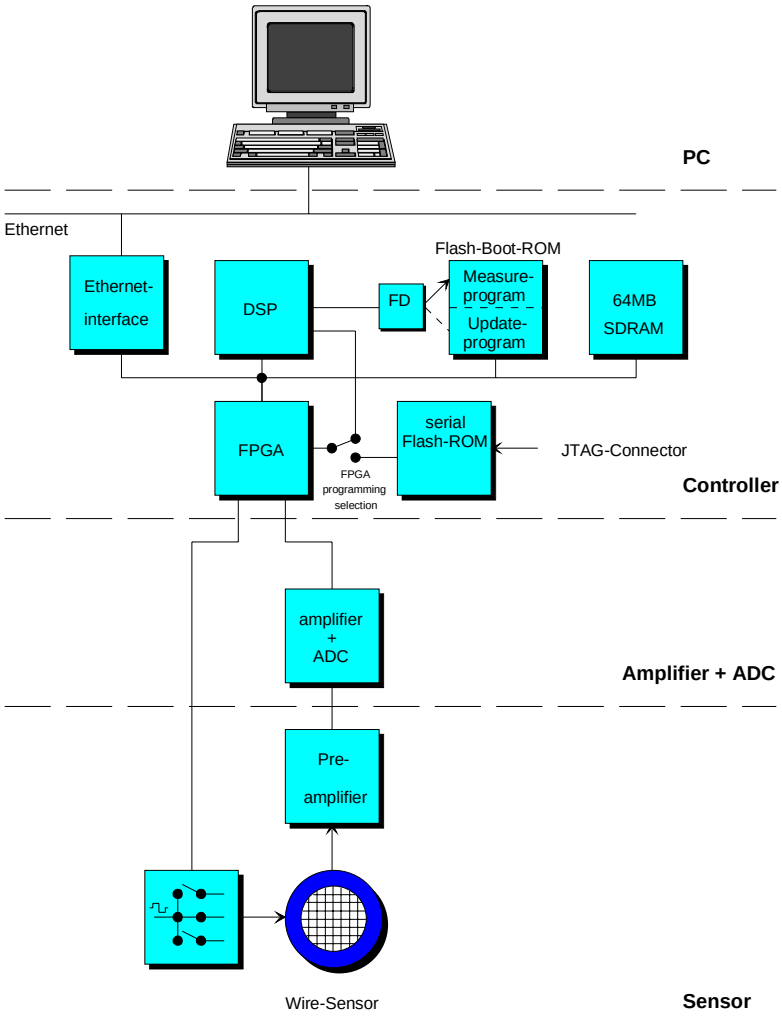

Fig 5: Structure of the second generation device with an imaging rate of 10 000 frames per second

While the measures 1 to 3 are necessary for a fast data transfer, measure 4 reduces the capacitive loads of the transmitter output cascades, the build-up time of the current-to-voltage cascades of the receiver amplifiers due to cable capacitance reduction and the amplitude of external disturbances. It furthermore eliminates the cable resistance between the transmitter and receiver cascades and the sensor electrodes, which results in a better suppression of cross-talk. Together with measure 5, a significant improvement of the properties of the system sensor excitation - sensor / pre-amplifier and of the signal quality, especially an increase of the signal-to-noise ratio was achieved. By measure 6, a reduction of the signal processing efforts were achieved.

For the preamplifiers the same operation amplifier circuits are used, as with the version for 1200 frames per second. By the arrangement of the sixteen output cascades for the control of the transmission electrodes and the sixteen current-to-voltage converters in separate, well screened housings directly plugged to the sensor and protected against electromagnetic disturbances, the necessary reduction in build-up time was achieved. The logic control of these remote functional units was implemented by a bus-system, which allows a simultaneous control of several of these units. In this way, the device is prepared for an operation with sensors of up to 64 x 64 measuring points.

The positive and negative amplitude of the excitation voltage for the transmitter electrodes is programmable, the pulse time can be set up to 3 µs for each half-period. The current-to-voltage converters dispose of an identical, binary amplification control in eight steps of a factor of two each. This is also identical with the 1200 Hz version of the signal acquisition unit. The connection between the output cascades of the transmitter electrodes and the current-to-voltage converters is realised through cables, the length of which is less critical than in case of the 1200 Hz version of the device, because the cables are driven by low-impedance cascades.

4 Evaluation of the measured data

4.1 Local instantaneous gas fractions and visualisation

The sensor delivers a sequence of two-dimensional distributions of the local instantaneous conductivity, measured in each mesh formed by two crossing wires. Local instantaneous gas fractions are calculated assuming a linear dependence between gas fraction and conductivity. For this, the measured conductivity values are related to calibration values obtained for plain liquid in the measuring plane. The result is a three-dimensional data array $\varepsilon_{i,j,k}$ where k is the number of the instantaneous gas fraction distribution in the time sequence. The indices correspond to co-ordinates x,y of the local measurement in the cross section and the current time t in the following way:

$$x = i \cdot \Delta x + x_0;\ y = j \cdot \Delta y + y_0;\ t = k \cdot \Delta t = \frac{k}{f_m} \qquad (1)$$

Δx and Δy are electrode pitches ($\Delta x = \Delta y = 3$ mm), f_m is the measuring frequency, $\Delta t = 1/f_m$ is the time step, x_0 and y_0 define the origin of the co-ordinate system. Any single value of $\varepsilon_{i,j,k}$ denotes, to which extend the corresponding fluid element is filled

with the gaseous phase. A visualisation can be carried out by assigning different colours to the local instantaneous gas fractions and plotting them in a grid that reflects the position of each individual control volume formed by crossing wires (Fig. 6, right side).

If the image is produced on the computer screen and refreshed with increasing time, a digital video sequence is generated.

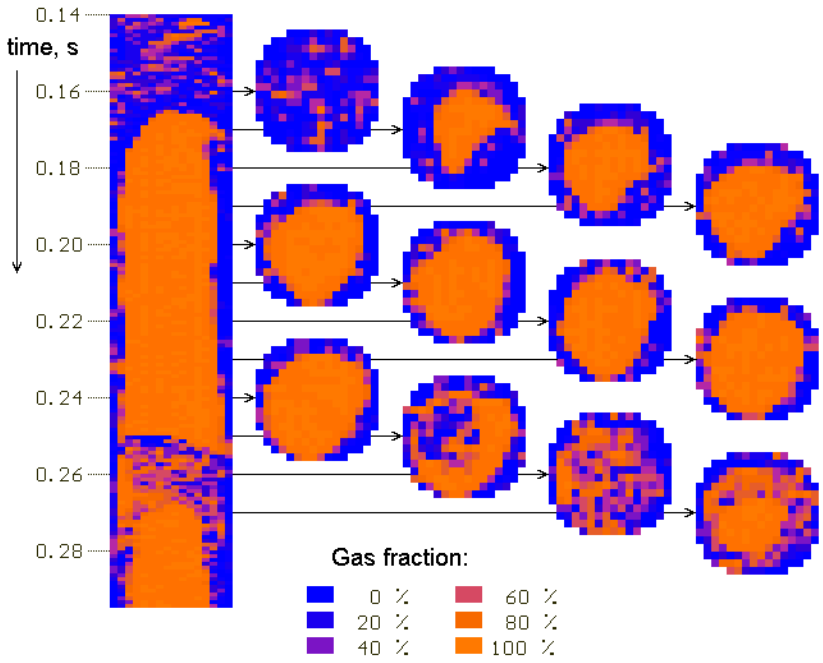

Fig. 6 Sequences of local instantaneous gas fractions obtained by the wire-mesh sensor in a vertical slug flow

A good inside into the flow structure is given by virtual sectional side-views. They are obtained by extracting the gas fraction distribution along the pipe diameter from the two-dimensional distribution and by stacking time series of these radial distributions as coloured bars in a vertical sequence (Fig. 6, left side). Additionally, in case of steady flow conditions, the time axis can be transformed into a virtual z*-axis by scaling it with the average phase velocity of the gaseous phase (see, for example, Fig. 11):

$$z^* = \overline{w_G} \cdot t \cong t \cdot J_G / \bar{\varepsilon} \tag{2}$$

The result is a virtual side-view of the flow structure. Characteristic structures, like bubbles and slugs are represented very illustratively.

4.2 Gas fraction profiles

A time-averaged two-dimensional gas fraction distribution is calculated as follows:

$$\bar{\varepsilon}_{i,j} = \frac{1}{k_{max}} \cdot \sum_{k=1}^{k_{max}} \varepsilon_{i,j,k} \tag{3}$$

where k_{max} is the number of instantaneous gas fraction distributions in the measuring sequence. A total average (void fraction) is obtained, when we average over the cross section:

$$\bar{\varepsilon} = \frac{1}{k_{max}} \cdot \sum_{i=1}^{i_{max}} \sum_{j=1}^{j_{max}} \sum_{k=1}^{k_{max}} a_{i,j} \cdot \varepsilon_{i,j,k} = \sum_{i=1}^{i_{max}} \sum_{j=1}^{j_{max}} a_{i,j} \cdot \bar{\varepsilon}_{i,j} \tag{4}$$

here i_{max} and j_{max} are the total numbers of electrode wires in both directions, $a_{i,j}$ are weight coefficients that express to which extend the given mesh [i,j] contributes to the total cross section of the sensor A_{sensor}. In the central region of the sensor holds $a_{i,j} = \Delta x \cdot \Delta y / A_{Sensor}$, while at the periphery the weight coefficients are less, they have to be calculated according to which extend the given mesh is partially covered by the circular border of the sensor (Fig. 7). Elements located outside the border of the sensor obtain weight coefficients equal zero.

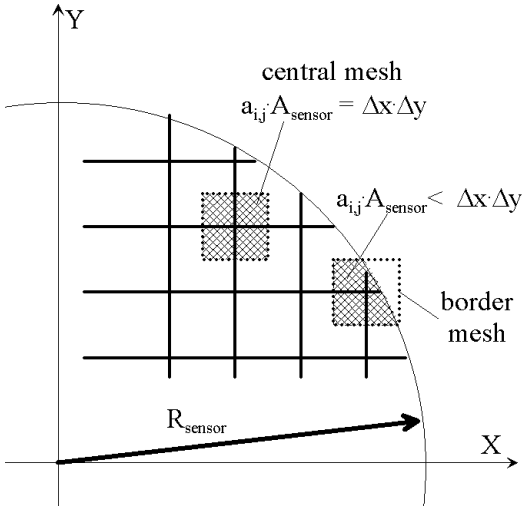

Fig. 7 Weight coefficients for averaging the gas fraction in the measuring cross section

Radial profiles can be calculated by dividing the radius into m intervals and introducing a radial step width $\Delta r = R_{sensor}/m$ and averaging $\bar{\varepsilon}_{i,j}$ over a ring-shaped domain, covering the radial interval $(m-1/2)\cdot\Delta r \le r \le (m+1/2)\cdot\Delta r$, see Fig. 8.

This is done using weight coefficients $a_{i,j,m}$, which characterise the common area of the mesh with the indices [i,j] and the ring with the number m and the central radius $m \cdot \Delta r$, related to the total cross section of the sensor A_{sensor}. The averaging can then be written as follows:

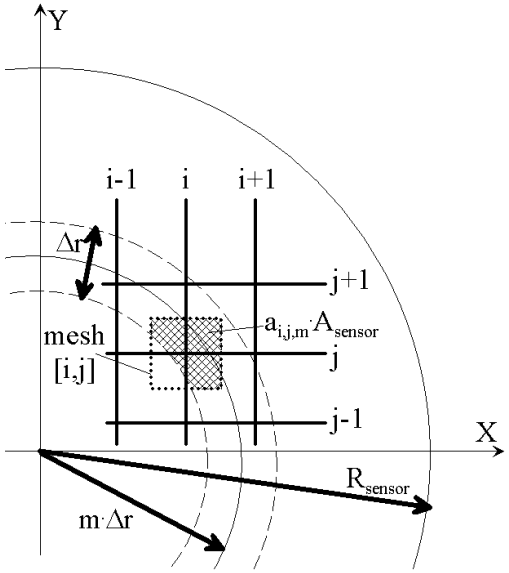

Fig. 8: Weight coefficients for calculating radial gas fraction profiles

$$\bar{\varepsilon}_m = \frac{1}{k_{max}} \cdot \sum_{i=1}^{i_{max}} \sum_{j=1}^{j_{max}} \sum_{k=1}^{k_{max}} a_{i,j,m} \cdot \varepsilon_{i,j,k} = \sum_{i=1}^{i_{max}} \sum_{j=1}^{j_{max}} a_{i,j,m} \cdot \bar{\varepsilon}_{i,j} \qquad (5)$$

The determination of the weight coefficients is based on simple geometric calculations, which does not require more detailed description.

4.3 Bubble size distributions

At moderate flow velocities, the high time resolution allows to perform a bubble size measurement, because individual bubbles are mapped in several successive frames. Furthermore, gas fraction portions belonging to bubbles the dimensions of

which exceed the electrode pitch are found in more than one mesh of the sensor. A detailed description of the method can be found in [6].

The bubble volume can therefore be derived by integrating over elements of the gas fraction distribution $\varepsilon_{i,j,k}$ belonging to the given bubble. The time necessary for the fluid element to travel through the sensor is inverse proportional to the velocity. The total gas volume flowing through one mesh of the sensor during the measuring period Δt equals $V_{G,x,y,t} = \varepsilon_{x,y,t} \cdot w_{G,x,y,t} \cdot \Delta x \cdot \Delta y \cdot \Delta t$. Here, $w_{G,x,y,t}$ is the axial component of the instantaneous local gas phase velocity. The volume can be written as:

$$V_{BL} = \Delta x \cdot \Delta y \cdot \Delta t \cdot \sum \varepsilon_{i,j,k} \cdot w_{G,i,j,k} \quad \forall [i,j,k] \in BL \tag{6}$$

From the bubble volume, an equivalent bubble diameters can be calculated:

$$D_{BL} = \sqrt[3]{\frac{6}{\pi} \cdot V_{BL}} \tag{7}$$

Before the volume can be calculated, it must be managed to identify, which elements [i,j,k] of the three-dimensional gas fraction distribution $\varepsilon_{i,j,k}$ belong to the bubble. A bubble is defined as a set of gas containing elements being in contact with each other, and which are surrounded by the liquid phase, i.e. by other elements, where the gas fraction equals zero. The task to obtain bubble size distributions can therefore be subdivided into the following steps:

- Identification of bubbles, i.e. assigning each element [i,j,k] to one of N bubbles or to the area of the solid liquid phase, which is done by a recursive fill algorithm.

- integrating the local instantaneous gas fraction over the elements belonging to the given bubble to obtain the bubble volume according to eq. (2) and transfer to an equivalent diameter, eq. (3),

- calculation of a statistical distribution with D_{BL} as variable by summing-up partial gas fractions $d\varepsilon / dD_{BL}$ carried by certain classes of bubbles.

It is still not possible to measure neither the local instantaneous gas velocity $w_{G,i,j,k}$ as a distribution over the cross section nor the velocity of each individual bubble. For this reason, the velocity was approximated by the average gas phase velocity: $w_{G,x,y,t} \cong \overline{w_G} = J_G / \overline{\varepsilon}$, i.e. non-uniformity over the cross section and fluctuations in time are neglected. This is a satisfying approximation for a rising turbulent two-phase flow in a vertical tube, in case of forced convection.

The method was tested by comparing the wire-mesh sensor data with high-speed video observations [6]. Based on a bubble size measurement using image processing techniques, the accuracy of the bubble size measurement was studied. Although the electrodes of the sensor cause significant bubble fragmentation, the recorded signal still represents the undisturbed shape and size of the bubbles.

4.4 Decomposition of gas fraction profiles according to bubble size classes

The bubble identification algorithm described in the previous chapter allows to identify, which elements [i,j,k] of the three-dimensional gas fraction distribution $\varepsilon_{i,j,k}$ belong to a given bubble.

Since the bubble diameter is known after carrying out the summation according eq. (6), it is possible to perform a decomposition of the distribution $\varepsilon_{i,j,k}$, a procedure which is illustrated in Fig. 9 (see also [7]). Here, a bubble diameter of 5.5 mm was chosen as threshold. If the resulting partial distributions are averaged applying eq. (4), partial radial gas fraction profiles can be obtained, which consider only bubbles from a given range of diameters.

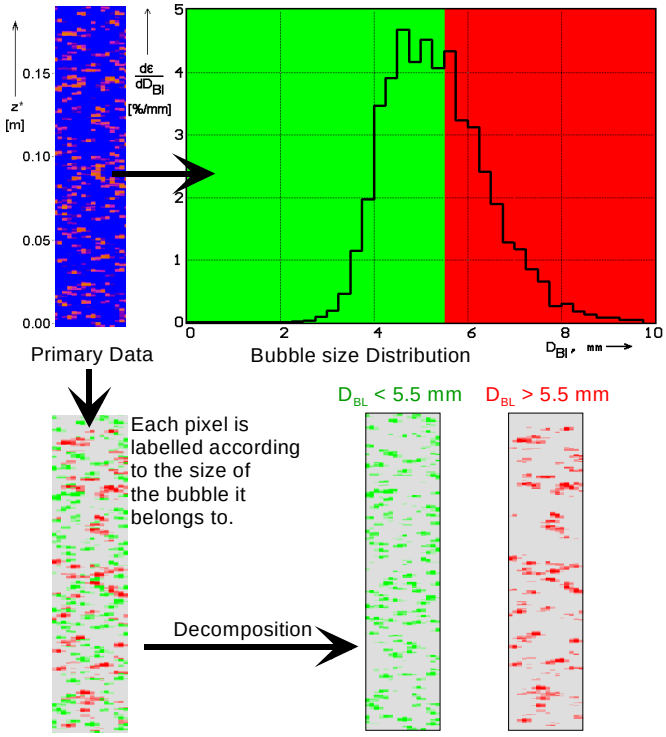

Fig. 9 Decomposition of sequences of instantaneous gas fraction distributions according to bubble size classes

(Flow conditions: J_{Water} = 0.4 m/s, J_{Air} = 0.06 m/s, L/D ≅ 60)

The left column represents a virtual sectional side view of the sequence of gas fraction distributions measured by the sensor. On the right side the bubble size distribution is plotted. The column below the virtual sectional view of the primary data is the result of colouring the bubbles according to their diameter: if the diameter is less than 5.5 mm, they were painted green, in the opposite case red. Now, the initial sequence can be divided in sequences of gas fraction distributions considering only bubbles with D_{BL} < 5.5 mm (column with only green bubbles) and D_{BL} > 5.5 mm (column with only red bubbles).These decomposed data sets are taken to calculate time averaged gas fraction distributions using eq. (4). Results of this kind are shown in section 5.

5 Bubble flow in a vertical tube

5.1 Experimental mock-up

The sensor was used to study the evolution of the bubble size distribution in a vertical tube of 51.2 mm diameter. A sketch of the test section is shown in Fig. 10. Experiments were carried out with an air-water flow at room temperature.

The superficial velocities were varied in the range of 0 < J_{Air} < 4 m/s and 0 < J_{Water} < 12 m/s. The distance between sensor and air injection was varied from 0.03 m to 3.5 m. This corresponds to related inlet lengths of 0.6 ≤ L/D ≤ 70.

Three different types of air injecting devices were used: (A) an array of 19 capillaries of 0.8 mm inner diameter, the ends of which were bent into the flow direction and equally distributed over the cross section, (B) 36 orifices in the tube side wall with 1 mm inner diameter and (C) 8 orifices in the side wall of 4 mm diameter.

5.2 Evolution of the flow pattern in case of a bubble-slug transition

An example of the results obtained with the large (4 mm) orifices is presented in Fig. 11. The superficial velocities of water and air corresponded to the region of slug flow. Virtual sectional views of the flow were constructed by extracting sequences of instantaneous gas fraction distributions over the diameter from the measuring cross section. These distributions were plotted in a stack of horizontal bars, beginning from the top of the image and moving downwards with increasing time. Using the known fluid velocity, the vertical axis was transformed from a time axis into a virtual height axis (z*). In the constructed image, the relation between width and height of the resulting column is kept equal to the relation between real tube diameter and scale of the z* axis.

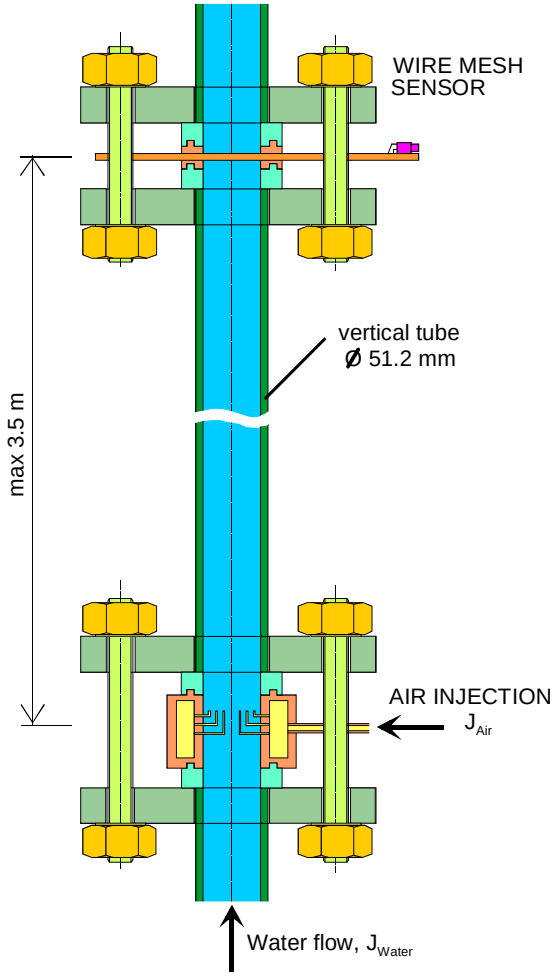

Fig. 10: Vertical test section with air injection and wire-mesh sensor (injection device A)

It is clearly visible that the transient process of slug formation continues over the entire length of the test section. Only at H=3033 mm (L/D ≅ 60) the expected slug flow has fully established. At the air injecting orifices, large bubbles are formed, which are still found close to the wall an a distance of H=30 mm above the injection. With growing distance, both coalescence and fragmentation occur and the bubbles start to move towards the center of the tube. In the end, a slug flow is established.

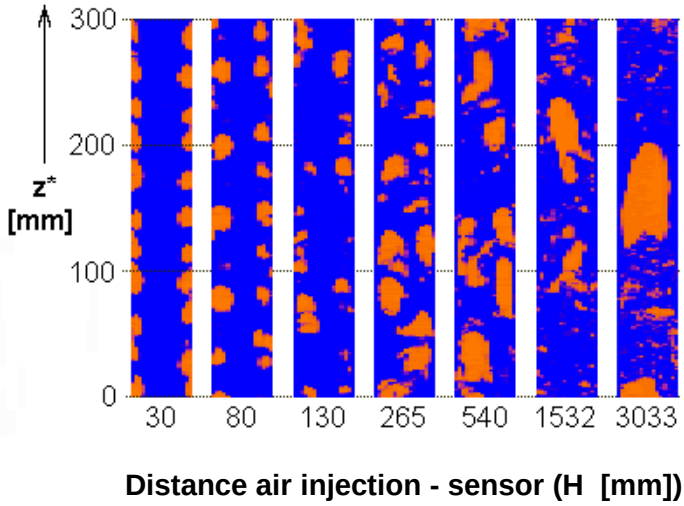

Fig. 11: Evolution of the flow pattern along a vertical tube, (J_{water}=1 m/s, J_{air}=0.5 m/s, H - distance air injection - sensor)

This is very well reflected by the bubble size distributions determined by the described method (Fig. 12). At the distance of 30 mm, an almost monomodal bubble size distribution with a peak at a bubble diameter of approximately 18 mm is found. With growing distance, both coalescence and fragmentation is observed. At H = 540 mm there is a bimodal bubble size distribution for the first time. The further growth of the slug bubbles leads to effective bubble diameters of over 50 mm, i.e. the bubbles take the shape of long plug bubbles at H = 3033 mm. At the same time, fragmentation is also continuing, leading to a growth of the quantity of small bubbles.

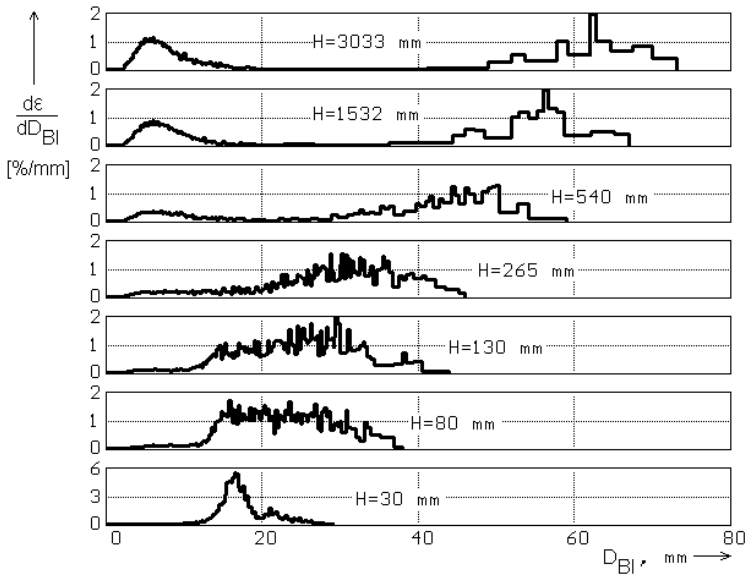

Fig. 12: Evolution of the bubble size distribution for the experiment in Fig. 5

It should be mentioned that the wire-mesh sensor is a very effective instrument to obtain the kind of information presented in Figs. 5 and 6. The measuring period to get one bubble size distribution with the shown quality is only 10 s. The application of needle probes, for example, would cause much more efforts, because longer integration periods and traversing of the probe would be necessary.

5.3 Result of the decomposition of gas fraction profiles according to bubble size classes

The decomposition of radial gas fraction profiles described in section 4.4 was applied to data obtained in an experiment with an air injection through the equally distributed capillaries (injection device A) and a variation of the inlet length from L/D ≅ 0.6 (H = 30 mm) to L/D ≅ 60 (H = 3133 mm). At the combination of superficial velocities of J_{Water} = 0.4 m/s and J_{Air} = 0.06 m/s, the measured bubble size distribution at H = 30 mm indicates, that all primary bubbles have an equivalent diameter smaller than 0.55 mm (Fig. 13, right side).

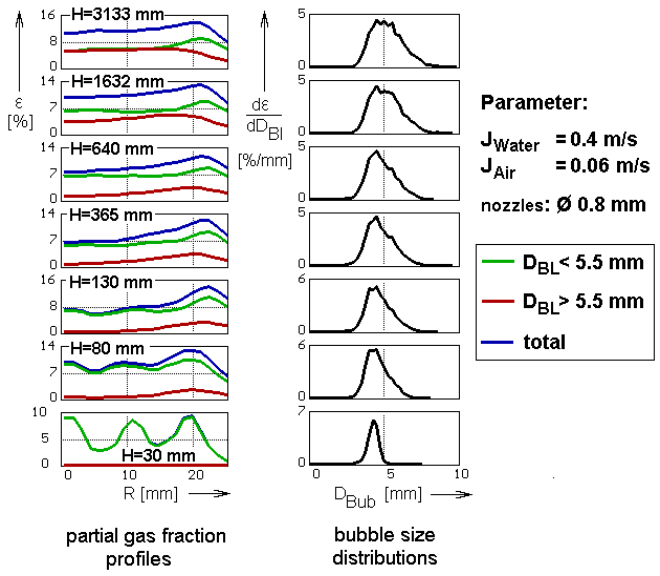

Fig. 13 Evolution of partial gas fraction profiles and bubble size distributions along the pipe

With increasing distance between air injection and sensor, the progressing bubble coalescence leads to the generation of bubbles greater than 5.5 mm.

When we look at the decomposed radial gas fraction profiles, the tendency of the small bubble fraction to move towards the wall is clearly visible. At H = 30 mm, the profile is still strongly determined by the gas fraction maxima found at the places where the capillaries are located. With growing distance, the gas fraction represented by the small bubble fraction shifts towards the wall. The increase of gas fraction near the wall leads to an intensification of coalescence, which leads to a generation of bubbles with $D_{Bl} > 5.5$ mm in this region. These bubbles experience an inverse lift force, pushing them towards the center of the pipe. At H = 3133 mm the equilibrium is nearly established. Here, we observe a pronounced wall peaking of the total gas fraction profile, caused by the peak of the partial gas fraction of the small bubble class. The large bubbles (D>5.5 mm) tend to form a central maximum. The mentioned processes are illustrated in Fig. 14.

A similar experiment at identical superficial velocities was carried out with the injection of air through the injecting device C (8 orifices of 4 mm diameter in the side wall). In this case, the primary bubbles are larger than 5.5 mm. Close above the injection they are found at the periphery of the pipe (Fig. 15), since they have been generated at the wall. With growing distance, a generation of both bubbles smaller than 5.5 mm and larger that 12.5 mm is observed.

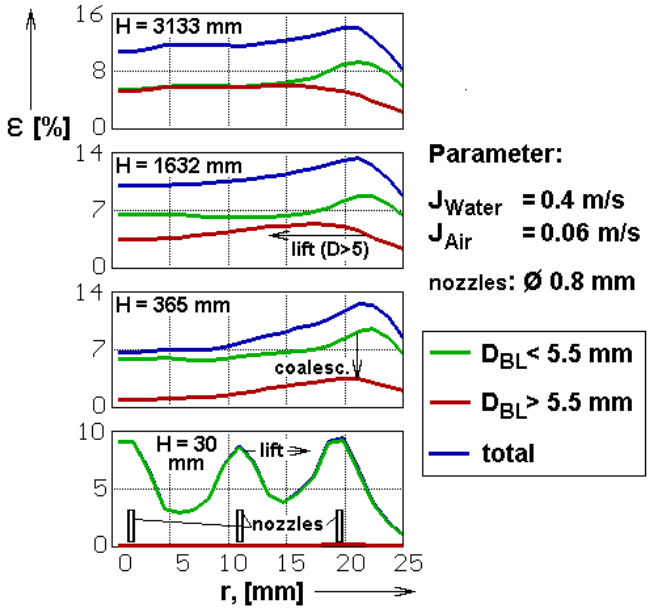

Fig. 14 Effect of coalescence and lift force to the evolution of gas fraction profiles

Since bubbles with a diameter less than 5.5 mm are not generated at the gas injection orifices, they must be the result of fragmentation events. In the same time bubble coalescence leads to the appearance of bubbles larger than 12.5 mm. The bubbles of both classes of large bubbles (5.5 mm ≤ D_{Bl} ≤ 12.5 mm and 12.5 mm ≤ D_{Bl}) are quickly shifted to the center of the pipe. At the end of the test section, the class of small bubbles does not show the expected wall peaking just because the fragmentation process is generating a large number of small bubbles in the center of the pipe, where the gas fractions are high. The more equal distribution of the small bubbles in comparison to the large bubble fractions is a hint to the tendency of the small bubble to move towards the wall.

A bimodal bubble size distribution characteristic for the transition from bubble to slug flow is established at the end of the test section. The inverse lift force transports the large bubbles to the centre of the pipe. The effect of coalescence, fragmentation and lift force is marked in Fig. 16.

It is worth a remark that the flow structure in the two examples shown in Figs. 13 - 16 is not identical at the end of the test section, despite of the identical superficial velocities of gas and liquid. Obviously, an inlet length of L/D ≅ 60 is still not sufficient to establish an equilibrium between bubble fragmentation and coalescence as well as with regard to the lateral movement of the bubbles. The flow pattern is still influenced by the kind of gas injection. We found that at higher superficial gas velocities the inlet length necessary to establish an equilibrium flow structure decreases [7].

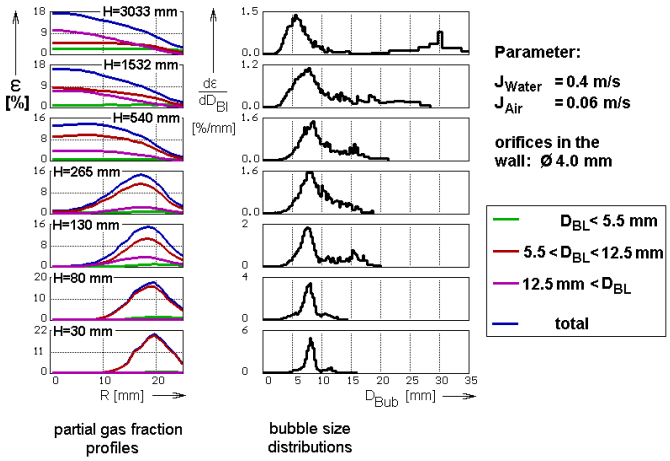

Fig. 15 Evolution of partial gas fraction profiles and bubble size distributions along the pipe, injection device C

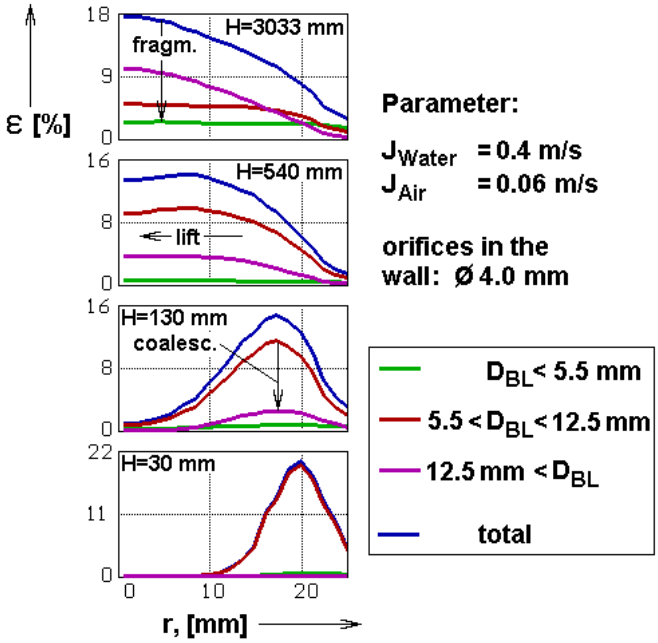

Fig. 16 Illustration of the main effects determining the evolution of gas fraction profiles

5.4 Flow pattern visualisation at high water and gas velocities

Up to now, the presented results in this paper were achieved by using the first generation of signal acquisition unit with a measuring rate of 1200 frames per second. The new capability of measuring 10 000 gas fraction distributions per second was recently used to visualise the transition from bubble to annular flow at a liquid velocity of 4 m/s. Fig. 17 illustrates the gained increase in resolution. For this purpose, a measurement taken at 10 000 frames per second was treated in a way that a resolution was reduced to that of the first generation of signal acquisition device. This was done by averaging 8 successive frames at the high resolution to obtain one of the low resolution. The corresponding virtual sectional view is shown on the left side of Fig. 17. In the middle, the same resolution is shown, but with a time axis enhanced to that of the right part of the figure, where the signal is plotted in the maximum available resolution. This kind of signal treatment allows to get a direct visual impression of the achieved increase in resolution.

To study the effect of transition from bubble to annular flow, the vertical test section in Fig, 10 was used. The measurements were carried out with a distance between air injection and sensor of H = 3033 m (L/D ≅ 60). The results of an increase of the superficial air velocity from 1 m/s to 10 m/s at a constant superficial water velocity of J_{Water} = 4 m/s are presented in form of virtual sectional side views in Fig 18.

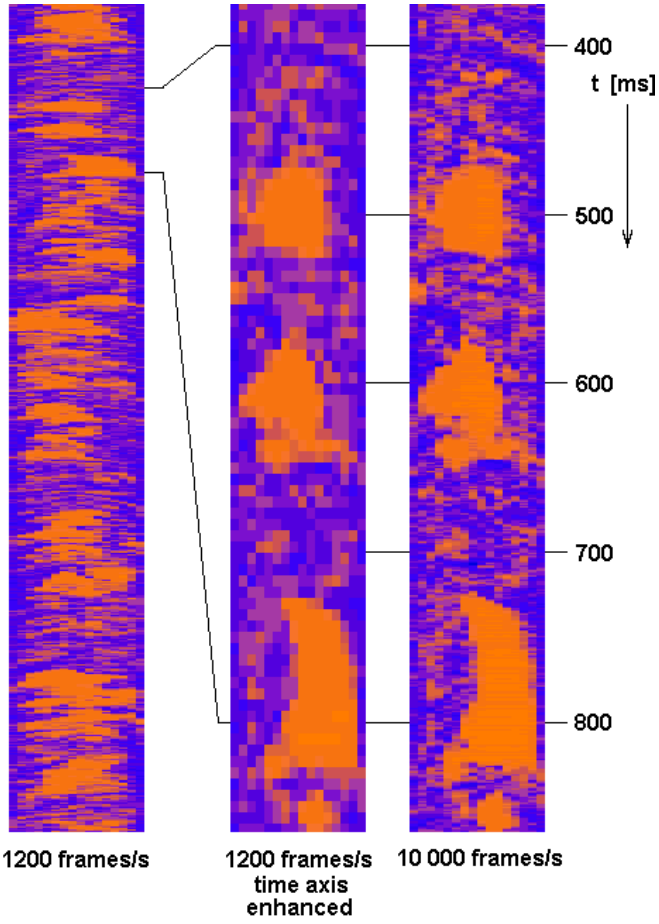

Fig. 17: Virtual side views of a fast slug flow obtained at different measuring rates, resolution increase gained by the 10 000 Hz device

At J_{Air} = 1 m/s the flow regime is still bubble flow. At J_{Air} = 2 m/s the generation of large bubbles due to coalescence is clearly visible. In the range of about 4 m/s superficial air velocity, periodic structures are observed, which remind gas plugs found under slug flow conditions. Compared to plugs at lower water velocities (see Fig. 11, H = 3033 m), these structures are strongly deformed by the action of the turbulent velocity field. When the gas flow rate is further increased to J_{Air} = 10 m/s, the flow pattern becomes really churn-turbulent. In detail, we observed, that the periodic structures dissolve, and an gas path is formed, which oscillates around the axis of the tube. This gas channel is interrupted from time to time by a region of higher water content. If can be stable for periods of about 20 - 50 ms.

According to classical flow maps, all the regimes shown in the Figs. 18 belong to the so-called "churn-turbulent" region. By the help of the high resolution of the wire-mesh sensor, we were able to identify plug-like periodic structures in the transition region between bubble and annular flow.

The air supply of the test facility does not allow a further increase of the air flow rate. In order to further approach the annular flow pattern, the water flow rate was decreased at a constant superficial air velocity of 10 m/s. The result is shown in Fig. 19.

The decrease of the superficial water velocity leads to a continuous extension of the gas channel in the center of the pipe within the cross section as well as in length. At a superficial water velocity of 1 m/s, a wispy-annular flow is observed. The wisps appear with a frequency of approximately 3 Hz, the sections of annular flow between the wisps is therefor approximately 3 m long ("Eulerian" length). On the right side of Fig. 19, the structure of one of such a wisp is shown.

6 Conclusion

The wire-mesh sensor provides detailed information about the structure of the two-phase flow. It is successfully used to visualise the air-water flow in a vertical pipeline. From the primary measuring data it is possible to obtain void fraction profiles as well as bubble size distributions. Experiments were carried out to study the evolution of the flow structure with growing distance from the gas injection. The bubble size distributions clearly show the effect of coalescence and fragmentation.

The decomposition of radial gas fraction profiles according to bubble-size classes allows to study lift force effects. The difference in the behaviour of small and large bubbles in connection with the change in sign of the lift force, which was predicted by Tomiyama [5], was observed by he new measuring method in a realistic multi-disperse two-phase flow.

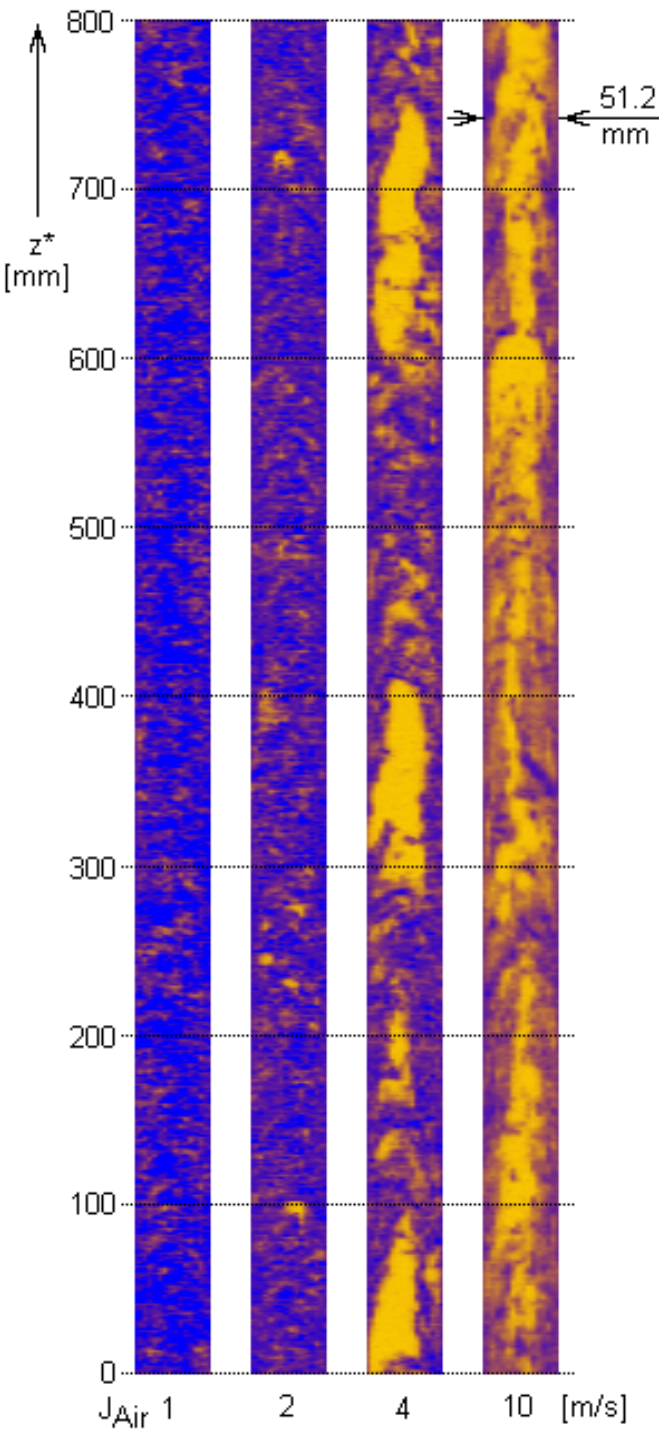

Fig. 18: Virtual sectional views obtained from a vertical air-water flow at J_{Water} = 4 m/s, recorded with the wire-mesh sensor at 10 000 frames per second

The results have furthermore shown, that the coalescence intensity depends from the local gas fraction. In case of the injection of bubbles small enough to be driven towards the wall, the formation of large bubbles starts in the layer close to the pipe wall, where the gas fraction distribution develops the well-known wall peak. The generated large bubbles experience an inverse lift force and are travelling towards

the centre. In case of a high enough gas fraction in the center, there can be a source of small bubbles in the central region, which afterwards start to move in direction towards the wall.

A new generation of wire-mesh sensor signal acquisition unit was applied to visualise the air-water flow in the vertical pipe for the first time. The achieved time resolution of 10 000 frames per second allows unique insights into the flow structure at higher superficial velocities. It was found that even in the region of so-called churn-turbulent flow, the transition from bubble to annular flow covers an intermediate state with periodic structures, similar to gas plugs found in the vertical slug flow. These plugs are strongly deformed by the turbulent velocity field.

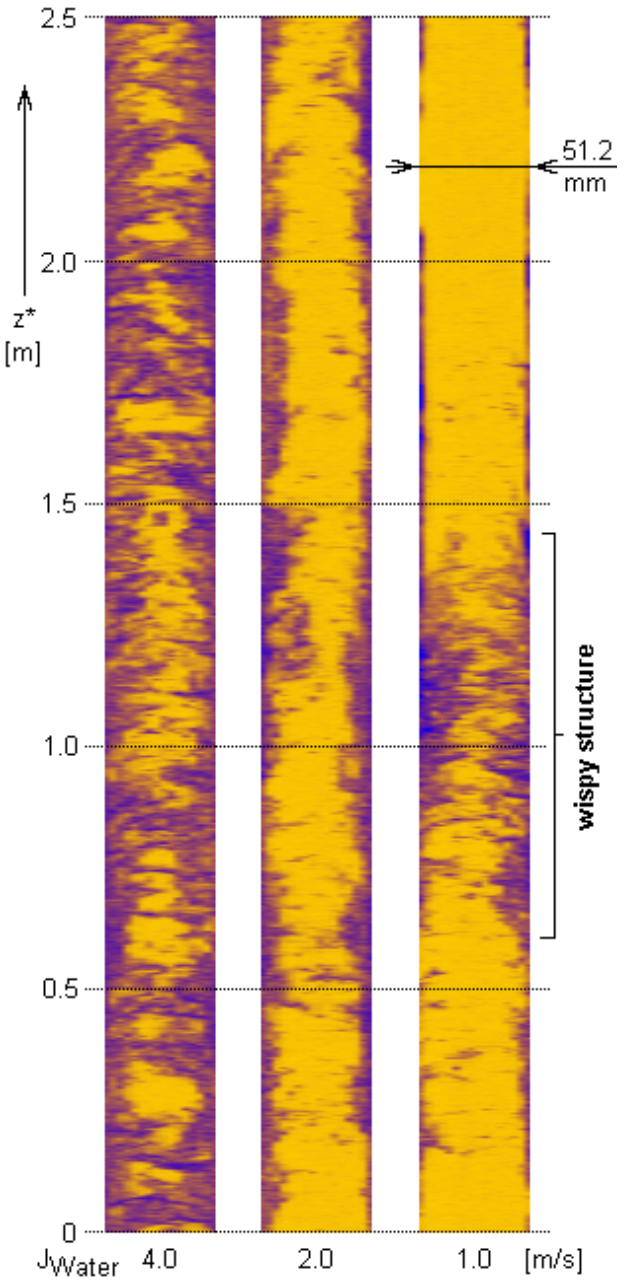

Fig. 19: Transition to a wispy-annular flow by decreasing the superficial water velocity at a constant superficial air velocity of J_{Air} = 10 m/s

7 Nomenclature

sign	unit	denomination
BL	(index)	bubble
D	m	diameter
f_m	Hz	meas. frequency
H	m	height
i,j,k	-	indices
J	m/s	superficial velocity
L	m	length
t	s	time
V	m³	volume
w	m/s	velocity
x,y,z	m	co-ordinates
Δ	-	difference
ε	1	gas fraction
*	-	virtual

8 References

[1] I. D. Johnson: Method and Apparatus for Measuring Water in Crude Oil, United States Patent, No 4,644,263, Date of Patent: Feb. 17, 1987.

[2] N. Reinecke, M. Boddem, G. Petritsch, D. Mewes: Tomographisches Messen der relativen Phasenanteile in zweiphasigen Strömungen fluider Phasen, Chem. Ing. Tech. 68 (1996) 11, S. 1404-1412.

[3] H.-M. Prasser, A. Böttger, J. Zschau (1998), A new electrode-mesh tomograph for gas-liquid flows, Flow Measurement and Instrumentation 9, 111-119

[4] D. Peters, G. Pietzsch, H.-M. Prasser, W. Taubert, M. Trepte, J. Zschau, Wire-Mesh Sensor - now 10,000 Frames per Second, Institute of Safety Research, Annual Report 1999, FZR-284, Feb. 2000, ISSN 1437-322X, pp. 15-18

[5] A. Tomiyama: Struggle with computational bubble dynamics, Third International Conference on Multiphase Flow, ICMF'98, Lyon, France, June 8-12, 1998.

[6] H.-M. Prasser, D. Scholz, C. Zippe: Bubble Size Measurement using Wire-Mesh Sensors, Flow Measurement and Instrumentation (submitted).

[7] H.-M. Prasser, E. Krepper, D. Lucas: Fast wire-mesh sensors for gas-liquid flows and decomposition of gas fraction profiles according to bubble size classes, Second Japanese-European Two-Phase Flow Group Meeting, Tsukuba, Japan, September 25-29, 2000.